

Sources of Quasi-periodic Pulses in the Flare of 18 August 2012

A. Altyntsev¹ · N. Meshalkina¹ · H. Mészáros² ·
M. Karlický² · V. Palshin³ · S. Lesovoi¹

Received: 9 February 2015 / Accepted: 5 January 2016 / Published online: 9 March 2016
© Springer Science+Business Media Dordrecht 2016

Abstract We analyzed spatial and spectral characteristics of quasi-periodic pulses (QPP) for the limb flare on 18 August 2012, using new data from a complex of spectral and imaging instruments developed by the Siberian Solar Radio Telescope team and the *Wind/Konus* γ -ray spectrometer. A sequence of broadband pulses with periods of approximately ten seconds were observed in X-rays at energies between 25 keV and 300 keV, and in microwaves at frequencies from a few GHz up to 34 GHz during an interval of one minute. The QPP X-ray source was located slightly above the limb where the southern legs of large and small EUV loop systems were close to each other. Before the QPPs occurred, the soft X-ray emission and the *Ramaty High Energy Solar Spectroscopic Imager* signal from the energy channels below 25 keV were gradually arising for several minutes at the same location. It was found that each X-ray pulse showed a soft-hard-soft behavior. The 17 and 34 GHz microwave sources were at the footpoints of the small loop system, the source emitting in the 4.2–7.4 GHz band in the large system. The QPPs were probably generated by modulated acceleration processes in the energy-release site. We determined the plasma parameters in

✉ N. Meshalkina
nata@iszf.irk.ru

A. Altyntsev
altyntsev@iszf.irk.ru

H. Mészáros²
hana.meszarosova@asu.cas.cz

M. Karlický
marian.karlicky@asu.cas.cz

V. Palshin
val@mail.ioffe.ru

S. Lesovoi
svlesovoi@gmail.com

¹ Institute of Solar-Terrestrial Physics SB RAS, Lermontov st. 126A, Irkutsk 664033, Russia

² Astronomical Institute of the Academy of Sciences of the Czech Republic, 25165 Ondřejov, Czech Republic

³ Ioffe Physical Technical Institute, St. Petersburg 194021, Russia

the radio sources by analyzing the spectra. The microwave pulses might be explained by relatively weak variations of the spectral hardness of the emitting electrons.

Keywords Radio emission, active regions · Oscillations, solar · X-Ray bursts, association with flares

1. Introduction

Solar flares are known to produce large quantities of accelerated electrons. The location and physical properties of the acceleration region of high-energy electrons are not well understood, however. Hence, determining the properties of an acceleration region from spatially resolved observations of flare emission currently is actively studied. In particular, it is important to study events that show a quasi-periodic behavior of hard X-rays and microwaves (MW) on timescales of several seconds. The periodicity behaviors in X-ray/MW may reveal the characteristic timescales of processes in the source region.

The nature of quasi-periodical pulses (QPP) is under debate; nevertheless, two basic mechanisms for fluctuating QPP have been proposed. One mechanism relates the phenomenon to changes of plasma parameters in microwave (MW) sources as a result of magnetohydrodynamic (MHD) oscillations in flare loops. Sausage, kink, torsion, and slow sound modes are typically considered (*e.g.* Roberts, Edwin, and Benz, 1984; Nakariakov and Melnikov, 2009). In this approach, the X-ray oscillations appear as a result of variations of particle precipitation, which can be caused by a modulation of pitch angle and mirror ratio in the loop footpoints. In microwaves, we can observe MHD modulations of source parameters such as the magnetic field, plasma density, temperature, electron distribution function, and the source dimensions (*e.g.* Aschwanden, 1987; Grechnev, White, and Kundu, 2003). A quantitative study of the observable MW signatures of the MHD oscillation modes in coronal loops was performed by Mossessian and Fleishman (2012). On the other hand, the efficiency of particle acceleration mechanisms may depend strongly on changes of plasma parameters in acceleration sites, and the X-ray and microwave emission can therefore clearly respond to relatively weak disturbances that are associated with MHD oscillations (*e.g.* Asai *et al.*, 2001; Kallunki and Pohjolainen, 2012). In all of these cases we expect the QPP periods to be similar to the periods of the MHD oscillations or their harmonics (Nakariakov *et al.*, 2006). The main problem is that the oscillation mode cannot be identified because, as a rule, available observations do not determine plasma and geometric properties of the oscillation loops.

In the second mechanism, QPPs are considered to be caused by some intrinsic property of the primary energy release (Nakariakov and Melnikov, 2009). Models with an electron-acceleration modulation naturally explain the simultaneity of the oscillations in different emission bands. Moreover, the high modulation of QPP can be easily achieved because it is controlled by variations of the non-thermal electron density. The current-loop coalescence instability proposed by Tajima, Brunel, and Sakai (1982) and Tajima *et al.* (1987) belongs to this category. They have studied the current-loop coalescence instability by numerical simulation and showed that the stored magnetic energy can be explosively converted into particle kinetic energy. They also showed that the current-loop coalescence instability can produce QPPs with a period of about the Alfvén transit time “across” the current-loop. However, the verification of the theory was based on observations without spatial resolution, and the QPP loop geometry was unknown. For this type of mechanism, another scenario proposes that the QPP emission follows from plasmoids that are periodically distributed in space and are

generated by a tearing instability in the flare current sheet and the following coalescence (Kliem, Karlický, and Benz, 2000). The individual bursts should appear at different spatial locations, gradually progressing along the arcade. The hard X-ray data show that the position of footpoint-like paired sources of individual bursts moved along the arcade (*e.g.* Grigis and Benz, 2005; Nakariakov and Zimovets, 2011; Gruszecki and Nakariakov, 2011; Inglis and Gilbert, 2013; Yang *et al.*, 2009). The individual pulsations are emitted from footpoints of different magnetic loops. Acceleration (or injection) of the non-thermal electrons apparently occurred near the tops of these loops.

To identify the mechanisms of the QPP we need to know the geometry of the flare loops, the values of the magnetic field, the plasma density, and the temperature. X-ray and microwave observations complement each other, since the mechanisms and conditions for the generation of radiation are essentially different. The HXR emission is emitted from electrons with energies of up to a few hundred keV, while the microwave emission is generated by higher-energy electrons. The radio spectra are dependent on magnetic field properties in the QPP sources.

Several events have been studied in which the quasi-periodic pulsations have been seen simultaneously in microwaves and hard X-rays (*e.g.* Nakajima *et al.*, 1983; Aschwanden, 1987; Altyntsev, Grechnev, and Hanaoka, 1998; Asai *et al.*, 2001; Grechnev, White, and Kundu, 2003; Mészárosová *et al.*, 2006). The similarity of the light curves confirms that the electrons radiating in these electromagnetic emissions have a common origin. The spatially resolved microwave data provide important additional information not only about the spectral and spatial properties of the QPP events, but also about the magnetic field in the QPP sources.

Detailed studies of individual flares, which usually reveal peculiarities of specific flares, are essential to better understand the flare phenomena. In this article, we describe a detailed analysis of multiwavelength observations of a limb flare on 18 August 2012. We analyze the QPP using a broad data set including high temporal, spectral, and spatial resolution X-ray and microwave observations. The microwave emission of the flare was recorded by new spectropolarimeters and with the prototype of a multiwave radioheliograph developed by the Siberian Solar Radio Telescope team. We also used data recorded with the *Wind/Konus* (hereafter WK) γ -ray spectrometer onboard the Global Geospace Science *Wind* spacecraft. The instruments and observations are described in Section 2, the data are analyzed and discussed in Section 3, and the conclusions are drawn in Section 4.

2. Observations

A GOES M1.8 flare on 18 August 2012 occurred in the region NOAA 11548 (N19E86). Soft X-ray measurements made with the GOES-15 spacecraft showed that this flare started around 03:19 UT and achieved its maximum at 03:23 UT. The flare was well observed by the Siberian Solar Radio Telescope (SSRT), the ten-antenna prototype of the multifrequency Siberian radioheliograph, the Nobeyama Radioheliograph (NoRH), the *Ramaty High Energy Solar Spectroscopic Imager* (RHESSI) telescope, and the *Atmospheric Imaging Assembly* (AIA; Lemen *et al.*, 2012) onboard the *Solar Dynamics Observatory* (SDO). In addition, we used records of the total solar flux observed by the Solar Radio Spectropolarimeters (SRS), the Badary Broadband Microwave Spectropolarimeter (BBMS), and Nobeyama Radio Polarimeter (NoRP). To study its temporal behavior in hard X-rays, we included observations from RHESSI and the *Wind/Konus*, a γ -ray spectrometer.

2.1. Instrumentation

Microwave data with a spatial resolution of 5.7 GHz were acquired with the SSRT (Grechnev *et al.*, 2003; Kochanov, Anfinogentov, and Prosovetsky, 2013). The SSRT is a cross-shaped interferometer producing two-dimensional full-disk images every three to five minutes. At the time of the flare, the half-width of the SSRT beam was 19.6×20.3 arcsec. Using data from the ten-antenna prototype, we also studied locations and sizes of microwave sources at five frequencies (4.2, 4.9, 5.8, 6.9, and 7.4 GHz) with a cadence of 1.6 seconds (Lesovoi *et al.*, 2012). The estimates of the positions and sizes were made assuming that the sources are azimuthally symmetrical.

The flare was also observed by the NoRH, which has provided images of the solar disk at 17 and 34 GHz with a rapid cadence of 0.1 seconds (Nakajima *et al.*, 1994). A time series of maps was created using the Koshix software package (Hanaoka *et al.*, 1994). The angular resolution was 12.3×12.8 arcsec and 8.1×8.3 arcsec at 17 and 34 GHz during this event, respectively.

We used the HXR data obtained with RHESSI (Lin *et al.*, 2002) in the energy band 3–300 keV. We used the forward-fit (FWD) method and the OSPEX algorithm for imaging and spectra fitting, respectively. The FWD approach is very effective for sources with a relatively simple structure such as the one that we study here. The structure of the flare region was obtained with AIA.

We analyzed the dynamics of the microwave spectrum and the spatial characteristics of the QPP sources using the new complex of spectral instruments. The BBMS provides fine spectral measurements of the total solar emission (Stokes parameters I and V) in the 4–8 GHz band with a temporal resolution of 10 ms (Zhdanov and Zandanov, 2011). To measure the spectrum, we used data from the SRS spectropolarimeter (I and V fluxes at 16 frequencies: 2.3, 2.6, 2.8, 3.2, 3.6, 4.2, 4.8, 5.6, 6.6, 7.8, 8.7, 10.1, 13.2, 15.7, 19.9, and 22.9 GHz; the temporal resolution was 1.6 seconds).

The microwave flare spectra were also recorded with the Nobeyama Radio Polarimeters (Shibasaki, Ishiguro, and Enome, 1979; Nakajima *et al.*, 1985). The NoRP has recorded total fluxes in intensity and polarization at 1, 2, 3.75, 9.4, 17, 35, and 80 GHz with a temporal resolution of 0.1 seconds.

To study the hard X-ray temporal behavior, we also used data from *Wind/Konus* (WK). In the waiting mode, WK records a time history in three energy ranges [G1, G2, G3] with bounds 21–81 keV, 81–324 keV, and 324–1225 keV, with a temporal resolution of 2.944 seconds. In the triggered mode, the time history is measured in the same three channels with a resolution varying from 2 to 256 ms and a total record duration of 230 seconds, and 64 spectra are also measured in the 20 keV–15 MeV band. A detailed description of the experiment can be found in Aptekar *et al.* (1995), and a brief overview of solar-flare observations with WK is given in Palshin *et al.* (2014). We here used the 256 ms records in the G1, G2 ranges; the signal in the G3 range was too weak for this flare.

2.2. Total Flux Profiles

Light curves recorded during the flare in X-rays and microwaves are presented in Figure 1. The flare started in the soft X-rays at 03:19 UT and the GOES signals increased gradually during four minutes (panel a). A similar behavior was seen in the hard X-rays at energies below 25 keV (panel b). Clusters of frequency-drifting subsecond structures (see Figure 2) appeared at the beginning of the flare at frequencies of about 5 GHz. After this, hard X-ray and microwave emission (panels b, c) began to rise.

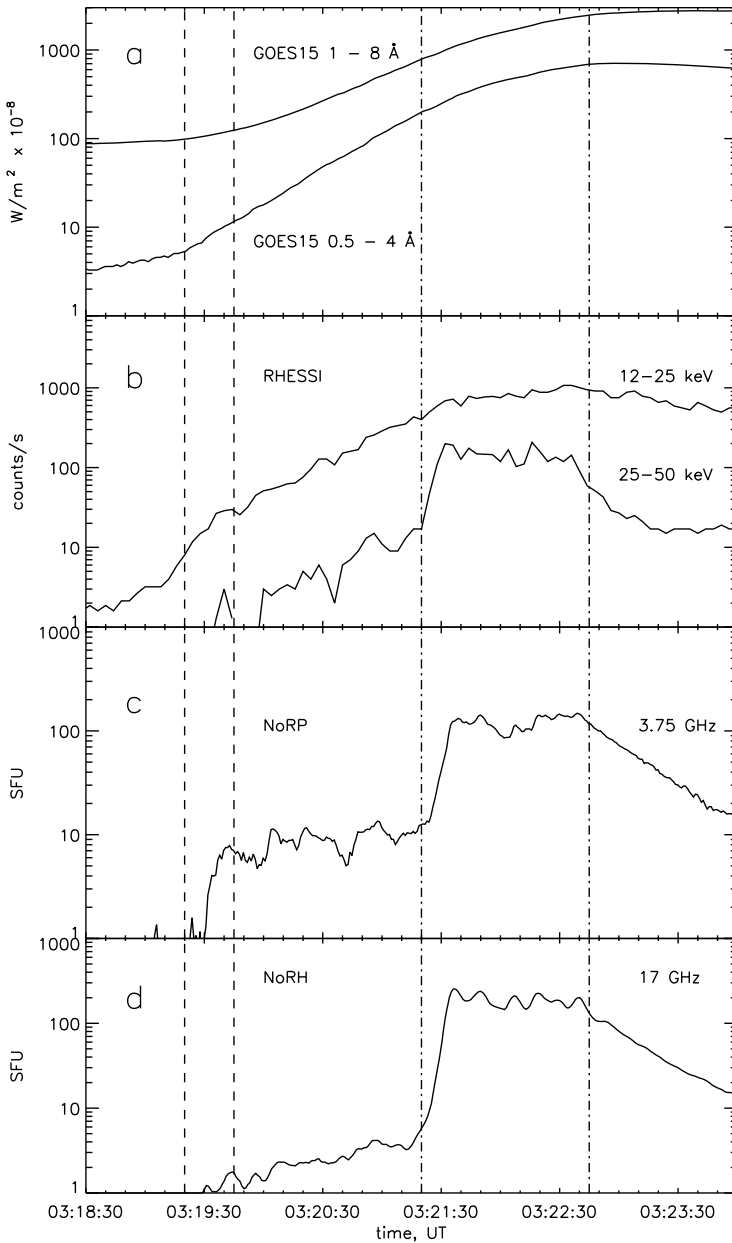


Figure 1 Soft (a) and hard (b) X-ray profiles together with microwave (c, d) fluxes. The dashed-vertical lines indicate the interval with the fine spectral structures (see Figure 2), the dash-dotted lines indicate the interval with the QPP (Figure 3).

After the flare emission sharply increased around 03:21:24 UT, a series of QPP occurred in higher-energy X-ray channels and microwave frequencies. During an interval of one minute, six prominent quasi-periodic pulses were recorded in hard X-rays and in mi-

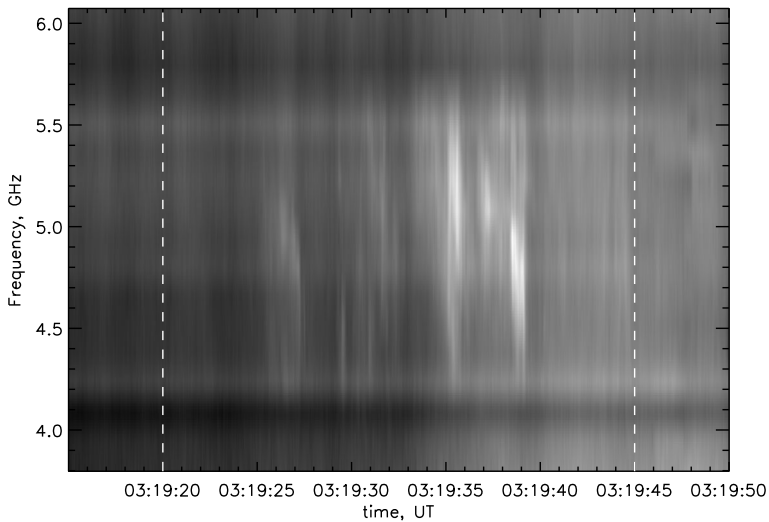


Figure 2 Portion of the dynamic spectrum, recorded with BBMS. The dashed-vertical lines indicate the interval with the fine spectral structure shown in Figure 1.

crowaves (panel d). We note that there was no apparent response in the GOES signals or in the low-energy RHESSI channel. This shows that QPP are related to non-thermal electrons.

The extended interval with the QPP is presented in Figure 3. The first four panels show the microwave profiles measured by the SRS and NoRP/NoRH. The accuracy of microwave measurements can roughly be seen from the minor difference between the independently measured profiles shown as solid and dotted curves in the first three panels in Figure 3. In the course of the QPP stage, two flux enhancements occurred at 3.75 GHz (Figure 3b) and lasted for about 30 seconds. The time intervals with enhancements are marked by the vertical-dashed lines. The QPP modulation was more pronounced at high frequencies. The polarization profiles are not shown because the polarization degrees did not exceed 0.05. The microwave spectrum slope $\gamma_{\text{MW}} = \ln(F_{17}/F_{34})/\ln 2$, determined by the ratio of fluxes at 17 and 34 GHz, is shown in Figure 3e. Again we can see the two distinct intervals in the behavior of γ_{MW} that correspond to the flux enhancements at the lower frequencies. During each interval, the index gradually decreased from $\gamma_{\text{MW}} = 2.9$ to 2.5 on a timescale of 60–70 seconds. Hereafter, we refer to these two intervals as the enhancements.

The hard X-ray profiles (G1, G2) measured with *Wind/Konus* are shown in panels f and g of Figure 3. The signal in the G3 range was too weak to allow a meaningful analysis. Similar to MW emissions, the WK light curve shows two sets of decreasing QPP. We note that the strongest X-ray pulses (numbers 1, 2, and 4) have a double or triple structure. The last panel (Figure 3h) presents the power-law index of the hard X-ray spectrum measured with RHESSI. The solid curve shows the natural logarithm of the WK hardness ratio (derived as the ratio of background-subtracted counts in the G1 and G2 ranges) multiplied by two. The temporal evolution of the index obtained from the fitting of the RHESSI spectra and the index obtained from the WK hardness ratio agree well.

The trends of the power-law indices γ_{X} during the enhancements (the dotted lines) showed that the spectrum softened with the exponential growth timescale of 60 and 70 seconds, just opposite to the trend direction of the microwave index γ_{MW} . The maxima of the QPP corresponded to the local γ_{X} minima.

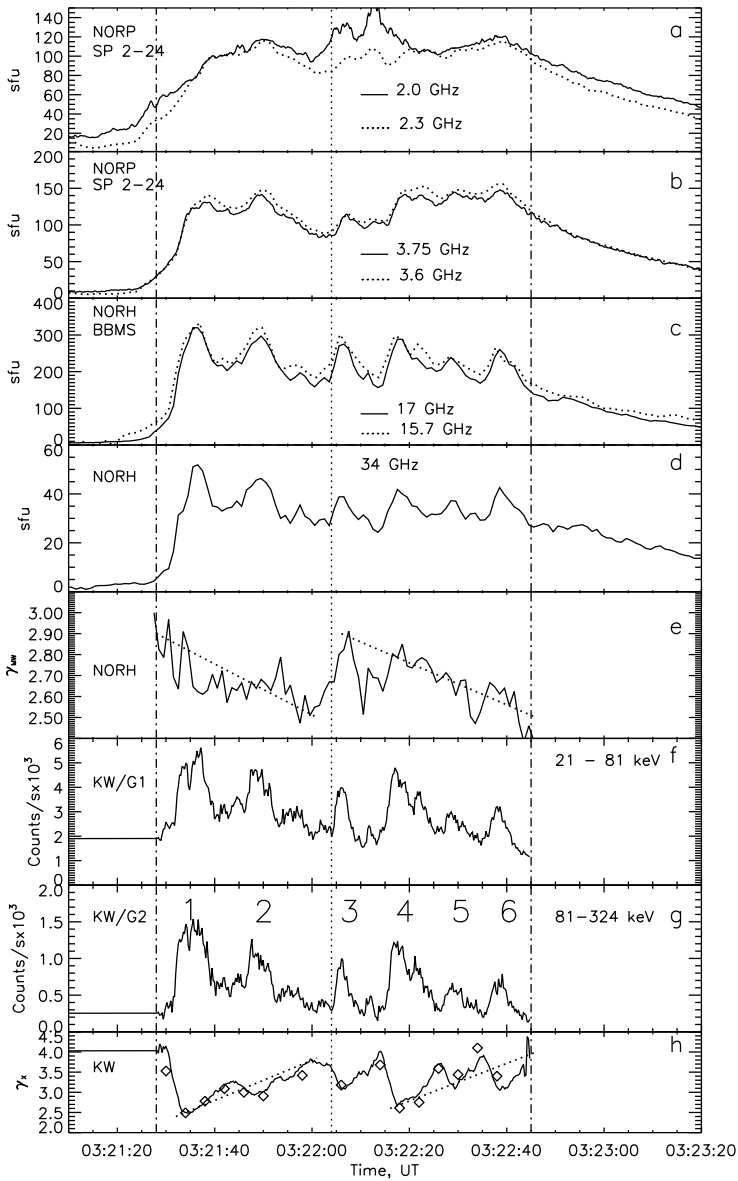


Figure 3 a–d) Brightness of microwave emission (solid: NoRP or NoRH, dotted: SRS) and hard X-rays (WK); e) power-law index calculated from the ratio of 17 GHz and 34 GHz fluxes; f, g) brightness of the HXR emission (WK); h) power-law indices of the hard X-ray spectra measured with the RHESSI (diamonds). The solid curve shows the natural logarithm of the WK hardness ratio [G1/G2] multiplied by two. The vertical dash-dotted lines mark the boundaries of the QPP interval, and the dotted line shows the beginning of the second enhancement. The prominent pulses are numbered in panel g. The inclined dotted lines (e, h) show index trends for each enhancement.

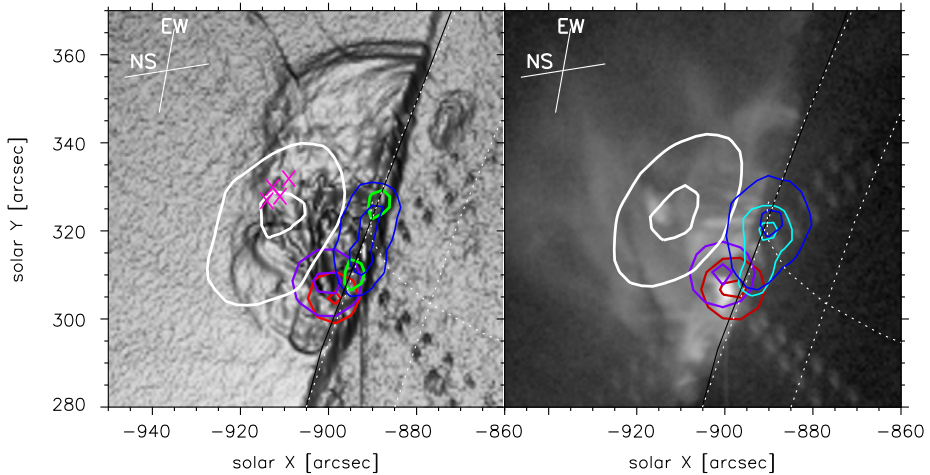


Figure 4 Flare structure before (left) and during (right) the QPP appearance. Background – EUV images at 211/94 Å (03:21:11 and 03:21:27 in the left and right panel, respectively). White contours show the continuum 5.7 GHz source (03:19/03:23, Stokes I), blue contours the continuum 17 GHz source (Stokes I , 03:21:13/03:21:25), violet contours the 12–25 keV X-ray sources (03:21:15/03:21:37), and red contours the 25–50 keV X-ray sources (03:21:15/03:21:37). The contour levels are 50 % and 90 %. In the left panel the green contours shows the 17 GHz sources of polarized emission at 90 % level; pink crosses depict source positions of the subsecond fine spectral emissions shown in Figure 2. In the right panel, cyan contours present the 34 GHz source at 03:21:25. The axes show arcseconds from the solar disk center. In the top-left corner, the cross shows the scan directions of the SSRT linear interferometers; the length of each line is the half-width of the SSRT beam.

2.3. Flare Configuration

The flare occurred in a rapidly time-varying complex of large and small EUV loops over the eastern limb (Figure 4). The EUV images observed at the different emission bands show a filament eruption from the flare region that began around 03:21:15 UT. After this, the microwave flux sharply increased at 03:21:24 UT. For X-ray and microwave emissions, two types of sources can be seen. One belongs to an apparent footpoint source as observed at 17 GHz (including the polarization emission at 17 GHz) and higher energies in X-ray such as ≥ 25 keV, while the other belongs to a coronal source as observed at 5.7 GHz and lower energies in X-ray. The microwave coronal source seen at 5.7 GHz is located at a height of 20 arcsec above the limb. The fine spectral structures were emitted from the region (pink crosses) inside the central part of the 5.7 GHz source.

The SDO/AIA 211 Å image shows that 5.7 and 17 GHz sources were located in different loops. This image was created using the Interactive Data Language (IDL) shade_surf procedure where the z -axis (not displayed here) presents the 211 Å emission intensity in a log 10 scale. The 17 GHz sources in polarization correspond to the footpoints of the UV loop, having a height of 12 arcsec. It is worth noting that the coronal source, as seen both in microwaves and X-rays, is co-spatial with the southern leg of a larger loop (closely spaced loop system).

The relative brightness of the sources at 17 GHz, where the QPP originate, changes considerably. The northern footpoint is strengthening (right panel). The 34 GHz source also appeared at this footpoint. After correcting for the beam width, the source sizes at 17 and 34 GHz were close to each other and varied between 6–9 arcsec during the QPP interval.

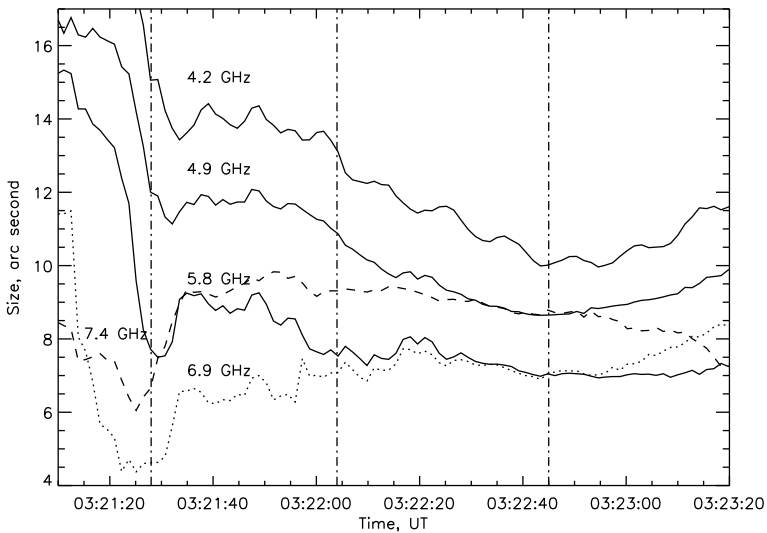


Figure 5 Size variations of the microwave source observed by the ten-antenna prototype in the frequency range 4.2–7.4 GHz. Dash-dotted lines mark the intervals with QPPs.

We did not find a relation between the QPP and the size variations. The structure of the X-ray sources did not change during the QPP stage.

The apparent sizes of the SXR sources obtained by the forward-fit algorithm are 10–15 arcsec. This is about twice as large as the bright patch at the same site seen in the SDO/AIA 94 Å image. The spatial resolution of the EUV images is high, and it is reasonable to assume that the bright patch with a size of about ten arcseconds provided the main contribution to the soft X-ray emission. From the GOES-15 signals it follows that the emission measure is $2.7 \times 10^{48} \text{ cm}^{-3}$ and the temperature is 16–18 MK during the QPP stage. We used the standard SolarSoft procedure to compute the emission measure and temperature from the GOES data. The RHESSI spectrum fitting reveals the parameters $(0.8\text{--}2.2) \times 10^{48} \text{ cm}^{-3}$ and 20–22 MK. Assuming that the source is a sphere of ten arcseconds diameter, we can estimate the plasma density in the X-ray source to be $(0.7\text{--}1.2) \times 10^{11} \text{ cm}^{-3}$. From the GOES measurement this value is roughly two times larger.

It was possible to study the spatial dynamics of the single 5.7 GHz sources at a number of frequencies using the ten-antenna interferometer observations. For a circular bright source, the accuracy of the size and displacement measurements is a few arcseconds. Observations show that the size behavior depends on time and frequency (Figure 5). At 4.2–5.8 GHz the FWHM angular size of the coronal source decreases to 8–14 arcsec during the first enhancement of the QPP stage. This process might belong to the phenomenon of contraction of flaring loops (Ji *et al.*, 2006; Ji, Huang, and Wang, 2007). The relation between the contraction and following oscillations appeared both in coronal loops and in X-ray/microwave emission and was studied in detail by Simoes *et al.* (2013). They interpreted the phenomena as persistent, semi-regular compressions of the flaring core region, which modulate the plasma temperature and emission measure. For the size of the 4.2 GHz source, we can see apparent oscillations, although there is no correlation between the size variations and QPP profiles at this resolution level. It is also worth noting that at higher frequencies (6.9–7.4 GHz), the sizes are smaller and do not change significantly with time.

Table 1 Results of cross-correlation and modulation amplitude.

	mod	K_{corr}	τ [s]
21–81 keV	0.26	0.95	< 0.3
81–324 keV	0.35	1.00	0
5.7 GHz	0.16	0.48	1.6
9.4 GHz	0.16	0.61	1.3
17 GHz	0.22	0.77	1.0
34 GHz	0.27	0.69	0.5

2.4. The QPP Properties

To characterize the QPP at different wavelengths, we calculated the modulation amplitude for each time profile as mod_v , which is the normalized modulation of the signal. The formula is given as follows, where t is the time in seconds, $T_{\text{QPP}} = 77$ seconds is the duration of the QPP interval, and F_v is the flux density at a given frequency,

$$\text{mod}_v = \left(\frac{1}{T_{\text{QPP}}} \int_0^{T_{\text{QPP}}} S_v^2(t) dt \right)^{1/2}, \quad \text{where } S_v(t) = \frac{F_v - \langle F_v(t) \rangle}{\langle F_v(t) \rangle}. \quad (1)$$

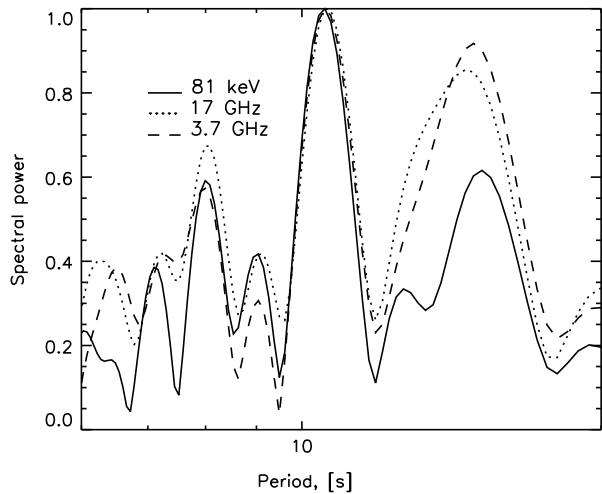
Using the time profile of 81–324 keV as a reference, we cross-correlated it with the time profiles of 21–81 keV and MW at 5.7, 9.4, 17, and 34 GHz. We obtained correlation coefficients [K_{corr}] and time delays [τ]; all results including the modulation amplitude mod are given in Table 1. We here used the NORP records with 0.1 second resolution. It can be considered that the signals in Table 1 are roughly ordered according to the energy of the emitting electrons, since the radio frequencies/X-ray energies are highly proportional to the electron energy. It is clear that the modulation amplitudes decreased with decrease of the energy of the electrons producing the X-rays and radio emission. We note that there was almost no time delay between the WK signals. From the sufficiently high correlation of the microwave emission with the X-ray pulses it follows that the upper microwave sources seen at 5.7 GHz are physically associated with the X-ray sources.

To find the QPP periods, we performed a Fourier analysis of the X-ray and microwave profiles during the QPP interval. Figure 6 shows the normalized power spectra for the hard X-rays at 81–324 keV, 17 GHz emission (from the northern footpoint of the low loop), and 3.75 GHz emission (from the large-loop source). All of these sources were oscillating with a common prominent period of 11 ± 1 seconds. Additional significant modes (above 0.5 level) were observed in microwaves, with periods of 8 and 15 seconds, and some subsidiary peaks. The modes with 8- and 15-second periods corresponded to beat frequencies that were produced by oscillations with periods of 10.5 seconds and 33 seconds. The last period is close to the duration of the enhancements described above.

The cross-correlation coefficients [K_{corr}] were high for the 21–81 keV and 17 GHz profiles. This confirmed that these sources were related to the same loop structure. The delay of microwave pulses that originated from the conjugate footpoint of the low loop was about one second. The 5.7 GHz emission was delayed by 1.6 seconds and the value of [K_{corr}] was lower than at 17 GHz. This is consistent with the assumption that they are localized in different magnetic loops.

The X-ray sources at different energies were located close to each other, and it is acceptable to describe the spectral index behavior by the ratio of the signals recorded with different energy channels. Figure 7 shows that the X-ray index changed in accordance with

Figure 6 Normalized power spectra of emission at different waves: *Wind/Konus* detector in the range 81–324 keV, and NoRP fluxes at 17 and 3.75 GHz. The squared magnitudes of the discrete Fourier transform (power spectrum) are normalized and presented in periods. The axis Y is in logarithmic scale.



the emission amplitude variations. During every pulse, the logarithmic value of the signal in the energy channel of 81–324 keV depended linearly on the logarithmic ratio of 21–81 and 81–324 keV signals in the rise as well as in the fall phases (Figure 7). The observed soft-hard-soft evolution of the spectral features indicates that every pulse can be considered as a primary energy release event.

The microwave spectrum at 03:21:37 UT (the peak of the first pulse) is shown in Figure 8. The spatial observations showed that this spectrum was mainly generated by two different sources: the upper source seen at 5.7 GHz and the near-limb source seen at 17 GHz. At high frequencies the spectrum was produced by the footpoint source with a size of 6–9 arcsec. Therefore we assume that the spectral slope in the optically thin regime was directly related to the power-law index of the electrons in the northern limb source. We have no reliable data on the low-frequency spectrum slope of this limb source, but it probably falls off sharply because the sources at 5.7 GHz and 17 GHz did not overlap in the radio maps.

The low-frequency part of the spectrum was emitted from the extended area of the large loops. The flat slope of the spectrum at frequencies below 10 GHz can be explained by the increase in emission area toward low frequencies (see Figure 5). Based on the ten-antenna prototype observations, we can estimate the spectrum emitted from the area of the 7.4 GHz source. To find the corresponding fluxes at 6.9, 5.8, 4.9, and 4.2 GHz, we multiplied the observed fluxes by a factor of $(6/D)^2$, where D was the size at the given frequency in arcseconds and six arcseconds was the source size at a frequency of 7.4 GHz. The recalculated flux values are shown by crosses in Figure 8. The necessity of taking the changing size into account to interpret the low-frequency part of a spectrum has been emphasized by a number of articles (see, for example, the review by Bastian, Benz, and Gary, 1998; Kundu *et al.*, 2009 and Lee, Gary, and Zirin, 1994).

The key results of the observations are summarized as follows:

- i) The X-ray emission at all observed energies was produced over the flare at the place where the southern legs of the small and large loops were close to each other. The quasi-periodic pulses were observed in this source at photon energies above 25 keV. The QPP source seen at 17 and 34 GHz was located at the northern conjugate footpoint of the low loops. Below 10 GHz, the continuum emission, subsecond, and quasi-periodic pulses originated from the high flare loops.

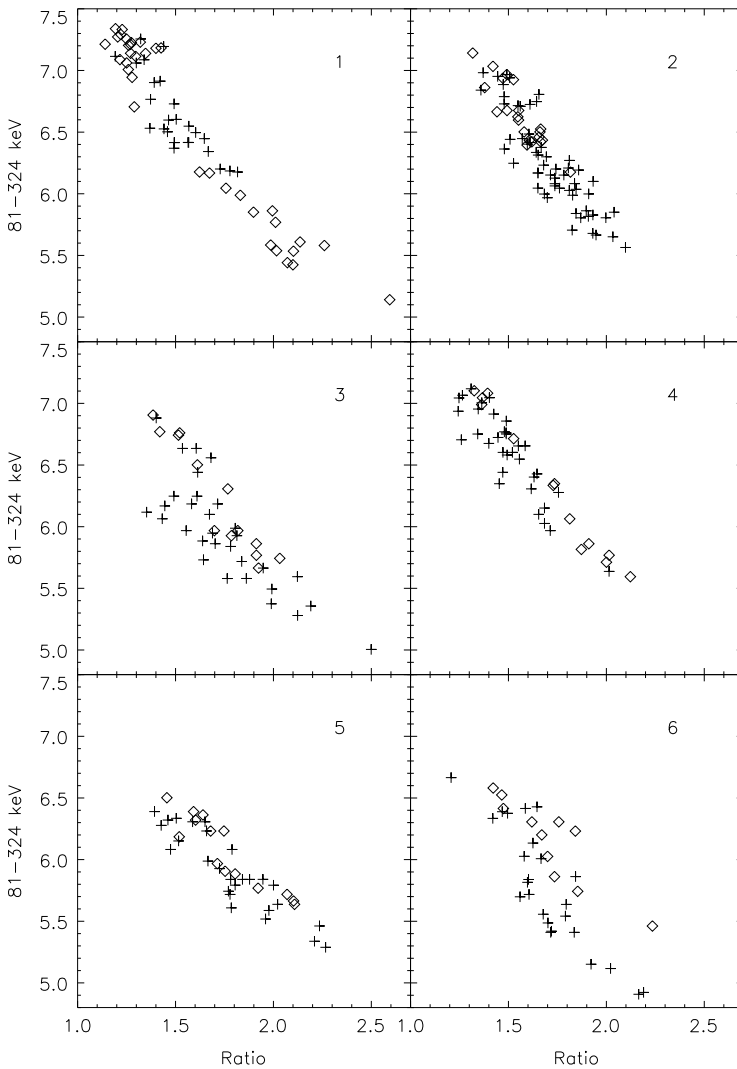
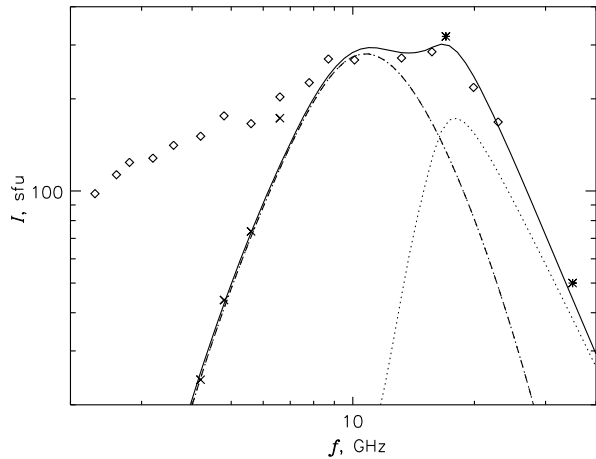


Figure 7 Soft-hard-soft behavior during the individual QPP. The panels show the logarithmic dependences of G2 signals on the logarithms of the G1/G2 signal ratio for individual pulses marked by numbers in Figure 3g. Diamonds correspond to the rise phase of the pulse and crosses to the decrease.

- ii) During the flare, the X-rays were characterized by thermal emission at energies below 25 keV. The emission measure and temperature gradually increased during the flare. In microwaves, the signatures of the non-thermal electrons appeared after the flare onset.
- iii) The sharp growth of the non-thermal electron population began several seconds after the filament eruption from the flare region. During the one-minute interval, the microwave and hard X-ray emissions displayed the QPP that were repeated in a period of 10.5 seconds and were highly correlated with each other. The background of QPP consisted of two successive intensity enhancements of 30–40 second durations with sharp rise edges and slowly decaying tails.

Figure 8 The MW spectrum during the peak of the first pulse (03:21:37) recorded by SRS (diamonds) and NoRH (asterisks). The normalized fluxes on the size of the source at 7.4 GHz are shown with crosses. The solid line indicates the result of spectrum fitting by two sources (dash-dotted line: upper source and dotted line: near-limb source).



- iv) The microwave QPP occurred later than the hard X-ray emission. The delays of the low-frequency pulses were up to 1.8 seconds at the upper source. At the limb source, the delays of the high-frequency pulses were a factor of two smaller.
- v) During the QPP the logarithms of the X-ray flux magnitude and the power-law index were related in a linear way. At long times there were different behaviors of the microwave and X-ray emissions. The power-law index of the HXR emission became gradually softer during the enhancements, but the microwave-spectrum slope became harder in that time.

3. Data Interpretation

3.1. Flare Configuration

To identify the QPP mechanism, we must determine the configuration of the flare loops and their plasma parameters. At first glance the locations of the flare sources (two high-frequency sources near the limb and one well above them) point to the so-called standard solar-flare model (CSHKP model). Furthermore, the flare was associated with the filament eruption. However, in the event under study, the sources did not vary, and the light curves at the footpoints were not delayed relative the top source. For the studied flare we could therefore assume two possible scenarios: i) with the reconnection at a location under the rising eruptive filament (Forbes, 2000), and ii) with the reconnection between interacting flare loops (Hanaoka, 1996). In the first scenario the upward motion of the filament should be seen in the 5.7 GHz images (Uralov *et al.*, 2002). However, no such motion was observed.

Although the standard flare scenario cannot be excluded, in the following interpretation of the X-ray and radio sources we assumed the scenario with the interacting loops and estimated the plasma parameters described in detail below. The flares in a configuration of two interacting current-carrying loops were first described by Hanaoka (1996). A number of flares were found to fit this quadrupolar geometry (see also Hanaoka, 1997; Nishio *et al.*, 1997; Aschwanden *et al.*, 1999). The energy-release interaction occurs between the small-flare loops system and large loops with footpoints close to each other (see cartoons in the articles cited above).

The sharp growth of energy release during the QPP stage can be excited by magnetic structure disturbances caused by the filament eruption from the flare region. The QPP similarity in X-rays and microwaves means that high-energy electrons are produced at the energy-release site and propagate over to the remote sites. Although the temporal modulation of the radio flux closely mimicked the hard X-ray pulses, the radio profiles were delayed by 0.5–1 seconds and 1.8 seconds. The 17 GHz emission is generated by relativistic electrons, and the transit time of 20 arcsec does not exceed 50 ms. The delays between the emissions from an energy-release site and some remote place can be increased by large pitch-angles of accelerated electrons. To provide a delay of one second, the pitch-angle must be in unrealistic ranges of a few degrees. Delays of this duration can be explained by energy-dependent trapping of emitting electrons. We note that for a one-loop configuration, a progressive delay of peaks emitted by higher-energy electrons is expected because of the effect of Coulomb collisions on the trapped electrons (Bai, 1982). In our case, the tendency was the reverse, and the delays were shorter at high frequencies. In the event under study, the QPP showed a soft-hard-soft X-ray behavior, which means that the relatively long delays at low frequencies cannot be explained by an energy-dependent injection. Clearly, all of these reasons confirm the suggestion that the flare had a two-loop configuration.

3.2. X-Ray Source

The size of the X-ray source was about 7–10 arcsec and did not exceed the free path of electrons with energies up to a few keV. In this source, the plasma was heated a few minutes before the QPP stage. At this stage we estimated the temperature as $T = 16 - 22$ MK and plasma density $n = (1-2) \times 10^{11} \text{ cm}^{-3}$. The hot plasma region was stable over the flare duration, and thus we estimated the magnetic-field strength in this source from the pressure balance as $B \geq \sqrt{16\pi k_B n T} \approx 100 - 170$ G, where k_B is the Boltzmann constant.

On the other hand, the magnetic value would not exceed this value considerably because the microwave emission from this source was weak. We estimated the radio emission of thermal electrons from the X-ray source site using the GX simulator developed by Fleishman and Kuznetsov (2010). It strongly depends on the value of the magnetic field (see Altyntsev *et al.*, 2012). Calculation showed that the 5.7 GHz flux should be above a detectable level of a few sfu for a magnetic field above 200 G. This means that the magnetic field probably does not exceed this value, and we use the value of 150 G in the calculations below.

The QPP appearance corresponded to the sharp increase of the non-thermal electron population. Before the QPP, the X-ray power law index was about $\gamma = 4.1$, and at the first pulse, γ decreased to 2.5. The QPP stage consisted of two X-ray enhancements with approximately equal durations of about 30 seconds. Each enhancement started by rising sharply, after which the background intensity gradually decreased. The X-ray hardness of background emission varied during these intervals from 2.5 to 3.7 on a timescale of 60–70 seconds (Figure 3h).

The duration of the rise and decay phase of the individual pulses was the same. The X-ray signals during the pulses varied in accordance with the spectral-index change, that is, the index had a soft-hard-soft behavior (Figure 7). Thus the trapping of the non-thermal electrons was weak in the interaction region.

3.3. The Microwave Sources

The spatially unresolved spectrum of the microwave emission at the first MW peak (03:21:37 UT) is shown in Figure 8. From the radio maps it follows that the spectrum consists of two main components that were emitted by the upper and limb sources at low

and high frequencies, respectively. First we consider the limb source producing the high-frequency slope of the spectrum.

The high-frequency source was seen at 17 and 34 GHz with sizes close to the NoRH beam widths. To model the spectrum, we used a source size of eight arcseconds and the fluxes recorded at 17, 19.9, and 22.9 GHz with the SRS and NoRH. The viewing angle of 85 degrees was taken from the flare-site longitude. We cannot determine the low-frequency part of the spectrum, but it must have rapidly decreased because this source was not seen in the 5.7 GHz images.

The dotted curve in Figure 8 presents the result of fitting the spectrum of the high-frequency source for the isotropic distribution of emitting electrons. From calculations using the code of Fleishman and Kuznetsov (2010), it follows that the spectrum slope at frequencies above 20 GHz can be produced by the gyrosynchrotron emission of electrons with energies of up to ≈ 0.8 MeV and a power-law index $\delta_{\text{MW}} = 3.55$. We note that the electron index [δ_{MW}] was practically equal to the index $\gamma_{\text{X}} = 3.53$ of the X-ray flux from the energy-release site. It is known that the flux index in the HXR target cannot be compared directly with the index determined from the microwave spectrum, since the radio emission is generated by the total number of radiating electrons in the coronal volume, not by a flux. The measured value is within the range of estimates $\delta_{\text{MW}} = \gamma_{\text{X}} + 1.5$ and $\delta_{\text{MW}} = \gamma_{\text{X}} - 0.5$ for the radio-emitting electrons, depending upon whether we assume a thick- or thin-target approximation for the X-ray source (e.g. White, Benz, and Christe, 2011).

To shift the spectrum turnover frequency up to 17 GHz and to suppress the emission at the lower frequencies, the magnetic field must be sufficiently strong in the source. In this fitting, the value of the magnetic field is taken to be 950 G. We note that Kosugi, Dennis, and Kai (1988) have found that the footpoint flare emission at 17 GHz is frequently generated by electrons with an energy of a few hundred keV in layers with a magnetic field of 900–1000 G. This means that the difference in microwave emission from the low-loop footpoints can be explained by the large difference of their magnetic fields. The complementarities of asymmetric hard X-ray and radio emission have been verified in several observations (e.g. Wang *et al.*, 1995).

During the enhancement, the average microwave index γ_{MW} slowly decreased on an exponential decay timescale of 220–270 seconds. The corresponding trends are shown by the dotted lines. Hereafter, we refer to these two intervals as the enhancements. It is remarkable that the long-term behavior of the emission at 17 and 34 GHz has the opposite tendency from the X-rays. Consequently, the acceleration process became weaker along the enhancements, but the trapping provided the slowly hardening of radio-emitting electrons.

For the limb source the microwave modulation levels were lower than in the hard X-rays by a factor of 1.5 (Table 1). There was no clear response of the MW index of the individual pulses. Spectrum modeling showed that the observed modulation level of 0.25 can be achieved when the power-law index of the emitting electrons varies by less than 0.05.

The low-frequency source was located well above the limb. Although the size of the source changed with frequency, it was possible to find the spectrum of a constant-size region using observations with the ten-antenna prototype. The corrected spectrum is shown by crosses in Figure 8 for the central region of six arcseconds. The dash-dotted curve depicts the result of matching the low-frequency part of the spectrum by gyrosynchrotron radiation based on the following assumptions about the parameters of non-thermal emitting electrons in the coronal source: the source area is taken to be equal to the area of a circle of six arcseconds in diameter, the magnetic-field vector direction to the line of sight is 85 degrees, and the energy spectrum has a power-law index of 3.25.

The optically thick part of the gyrosynchrotron spectrum is determined by the density of emitting electrons and the magnetic-field strength. In Figure 8 the spectrum model was obtained with a density of the emitted electrons of 10^9 cm^{-3} with an energy above 20 keV and a magnetic-field strength $B = 180 \text{ G}$. The last value was close for the magnetic-field estimate in the loop-interaction region. The density of the background plasma was $5 \times 10^{10} \text{ cm}^{-3}$. This density value is in accordance with observations of the fine structures at frequencies about 6 GHz near the top of the high loop. It is known that at such frequencies the fine spectral structures are produced by plasma mechanisms at a frequency of about the harmonic of the local Langmuir frequency (Meshalkina *et al.*, 2004). The modulation levels were lower than in the hard X-rays and limb source (Table 1). Spectrum modeling showed that a modulation level of 0.16 can be achieved when the variation of the power-law index of the emitting electrons is about 0.1.

3.4. The QPP Modulation

The source position did not change during the QPP stage. Therefore we cannot interpret the QPP using models in which the individual pulses correspond to different flare loops or spatially distributed plasmoids. Another peculiarity is that the smooth behavior of the quasi-thermal emissions from the site coincided with the QPP source. This means that there are no clear modulation-induced heating effects.

The power spectrum revealed the main X-ray modulation mode with a period of 10.5 seconds (Figure 6), which has been excited twice during the QPP stage with a separation of around 30 seconds. The microwave QPPs occurred with the same periodicity, but with the delays discussed above. We therefore consider that the pulsed acceleration, which occurred at a place close to the X-ray sources, was the driver of the broad-band emission pulses. During every pulse, the hardness of the X-rays has a soft-hard-soft behavior with an index modulation on the order of a few tenths. Grigis and Benz (2006) and Fleishman and Toptygin (2013) showed that a similar soft-hard-soft trend is expected from a transit-time damping stochastic acceleration model that included the escape of particles from the accelerator.

It is established that QPP can be caused by some intrinsic property of the energy-release process. The current-loop-coalescence instability proposed by Tajima, Brunel, and Sakai (1982) and Tajima *et al.* (1987) belongs to this category. The authors studied flares with QPP time profiles and found that their properties can be explained by development of current-carrying-loop coalescence instability. They showed that the main characteristics of the fast or explosive reconnection can be summarized as follows: i) a large amount of impulsive increase in the energy of particles, ii) appearance of quasi-periodic amplitude oscillations in nonthermal fluxes, and iii) double-peak (and triple-peak) structures in these oscillations. The multiple-peak behavior of the accelerated electrons is due to temporal variation of an electrostatic field in the coalescence process. All of these characteristics, including the sub-peaks in the strongest hard X-ray pulses, were observed in the flare under study. The oscillation period in the hard X-ray or microwave emission should be about the Alfvén transit time “across” the interacting loops. To estimate this timescale, we can take the values $n = (1-2) \times 10^{11} \text{ cm}^{-3}$ and the size of ten arcseconds determined above. The Alfvén transit time across the energy release site is close to the QPP period of ten seconds for a reasonable value of the magnetic field of 100–150 G. This estimate depends on the density values and on the size of the source, which are not known accurately, and the quantitative estimates are coarse.

On the other hand, such periodic processes can interact with MHD oscillations of the loops and can be affected by them (*e.g.* review by Nakariakov and Melnikov, 2009). Using

Table 2 Physical values of the flare loop.

Loop	Small	Large
Length [L : Mm]	17	70
Temperature [T : MK]	20	20
Density [n , 10^{11} cm $^{-3}$]	1.5	0.5
Magnetic field [B : G]	500	150
τ_{sausage} [s]	9.9	93
τ_{kink} [s]	$13/j$	$101/j$
τ_{slow} [s]	49	203
τ_{torsion} [s]	$13/m$	$101/m$

the source parameters for the loops determined above, we can roughly estimate the oscillation periods (Table 2, where m is the number of windings along the loop for torsional mode, $j - 1$ is the number of nodes for kink mode). The loop lengths are taken from the EUV image (Figure 4). To calculate the periods we used formulas (9–12) from Mossessian and Fleishman (2012). The main observed period of ten seconds can be excited in the small loop as sausage, kink, and torsional modes. In the large loops, such periods can be realized by the kink and torsion waves, but for too high harmonic numbers.

The global sausage mode is a compressive mode with a wavelength of twice the loop length. Magnetic-field perturbations are highest at the loop apex and lowest at the footpoints where the electron acceleration was modulated in the event under study. The mode is essentially compressible, and the quasi-thermal X-ray emission from the loop body should be modulated. Thus the observations do not support the sausage origin of the modulation. The kink and torsion modes are practically incompressible and more favorable.

The observed periodicity revealed one more timescale of about 30 seconds. Flux oscillations at low frequencies with the same period were seen from the flare beginning and might be related to low harmonics of the kink or torsion mode in the high loop. The kink oscillations should be seen because the sources shift in time. We did not observe any source-position movement corresponding to kink oscillations, but the spatial resolution of the measurements is probably not sufficient. The appearance of the pronounced QPP stage may be associated with the increase in the oscillation amplitude after the filament eruption.

4. Conclusion

The QPP observations in flares with relatively weak trapping of accelerated particles provide a perspective for studying primary-energy-release processes. In such events, these processes are well expressed, and periodicity properties provide supplementary keys with which the interpretations can be verified.

We here estimated the periods of the measured pulsations by taking the parameters from observations in the probable flare scenario of a two-loop coalescence. The spatial observation showed three QPP sources, whose positions did not change before and during the QPP stage. Every pulse can be considered as an elementary acceleration event with soft-hard-soft behavior. The X-ray index changed in accordance with the emission-amplitude variations.

The spatial observations at different frequencies showed that the low-frequency slope of the microwave spectrum can be explained by a change in the emission area. The characteristic timescales of the QPP are in accordance with estimates of the Alfvén transit time

across the interacting region. During the QPP stage, the microwaves were generated by non-thermal electrons through the gyrosynchrotron mechanism. The microwave pulses could be described as the response to the relatively small variations of the emitting electron hardness.

Acknowledgements We thank the anonymous referee for valuable comments. We are grateful to the teams of the Siberian Solar Radio Telescope, Nobeyama Radio Observatory, SDO/AIA, RHESSI, who have provided open access to their data. This study was supported by the Russian Foundation of Basic Research (15-02-01089, 15-02-03717, 14-02-91157), the Program of basic research of the RAS Presidium. The authors acknowledge the Marie Curie PIRSES-GA-2011-295272 RadioSun project. H. Mészárosová and M. Karlický acknowledge support by grants P209/12/0103 (GACR) and the research project RVO: 67985815 of the Astronomical Institute AS. The work was supported in part by the grants of Ministry of education and science of the Russian Federation (State Contracts 16.518.11.7065 and 02.740.11.0576). The *Wind/Konus* experiment is supported by a Russian Space Agency contract. The *Ramaty High Energy Solar Spectroscopic Imager* (RHESSI) is a NASA small explorer mission. AIA data are courtesy of NASA/SDO and the AIA science team.

Disclosure of Potential Conflicts of Interest The authors declare that they have no conflicts of interest.

References

- Altyntsev, A.T., Grechnev, V.V., Hanaoka, Y.: 1998, *Solar Phys.* **178**, 137. [ADS](#). [DOI](#).
- Altyntsev, A.T., Fleishman, G.D., Lesovoi, S.V., Meshalkina, N.S.: 2012, *Astrophys. J.* **758**, 138. [ADS](#). [DOI](#).
- Aptekar, R.L., Frederiks, D.D., Golenetskii, S.V., Ilynskii, V.N., Mazets, E.P., Panov, V.N., Sokolova, Z.J., Terekhov, M.M., Sheshin, L.O., Cline, T.L., Stillwell, D.E.: 1995, *Space Sci. Rev.* **71**(1–4), 265. [ADS](#). [DOI](#).
- Asai, A., Shimojo, M., Isobe, H., Morimoto, T., Yokoyama, T., Shibasaki, K., Nakajima, H.: 2001, *Astrophys. J.* **562**, L103. [ADS](#). [DOI](#).
- Aschwanden, M.J.: 1987, *Solar Phys.* **111**, 113. [ADS](#). [DOI](#).
- Aschwanden, M.J., Kosugi, T., Hanaoka, Y., Nishio, M., Melrose, D.B.: 1999, *Astrophys. J.* **526**, 1026. [ADS](#). [DOI](#).
- Bai, T.: 1982, *Astrophys. J.* **259**, 341. [ADS](#). [DOI](#).
- Bastian, T.S., Benz, A.O., Gary, D.E.: 1998, *Astron. Astrophys. Rev.* **36**, 131. [ADS](#). [DOI](#).
- Fleishman, G.D., Kuznetsov, A.A.: 2010, *Astrophys. J.* **721**, 1127. [ADS](#). [DOI](#).
- Fleishman, G.D., Toptygin, I.N.: 2013, *Mon. Not. Roy. Astron. Soc.* **429**, 2515. [ADS](#). [DOI](#).
- Forbes, T.G.: 2000, *Rev. Geophys. Space Phys.* **105**, 23153. [ADS](#). [DOI](#).
- Grechnev, V.V., White, S.M., Kundu, M.R.: 2003, *Astrophys. J.* **588**, 1163. [ADS](#). [DOI](#).
- Grechnev, V.V., Lesovoi, S.V., Smolkov, G.Ya., Krissinel, B.B., Zandanov, V.G., Altyntsev, A.T., Kardapolova, N.N., Sergeev, R.Y., Uralov, A.M., Maksimov, V.P., Lubyshev, B.I.: 2003, *Solar Phys.* **216**, 239. [ADS](#). [DOI](#).
- Grigis, P.C., Benz, A.O.: 2005, *Astrophys. J. Lett.* **625**, L143. [ADS](#). [DOI](#).
- Grigis, P.C., Benz, A.O.: 2006, *Astron. Astrophys.* **458**, 641. [ADS](#). [DOI](#).
- Gruszecki, M., Nakariakov, V.M.: 2011, *Astron. Astrophys.* **536**, A68, 7 pp. [ADS](#). [DOI](#).
- Hanaoka, Y.: 1996, *Solar Phys.* **165**(2), 275. [ADS](#). [DOI](#).
- Hanaoka, Y.: 1997, *Solar Phys.* **173**, 319. [ADS](#). [DOI](#).
- Hanaoka, Y., Shibasaki, K., Nishio, M., Enome, S., Nakajima, H., Takano, T., Torii, C., Sekiguchi, H., Bushimata, T., Kawashima, S., Shinohara, N., Irimajiri, Y., Koshiishi, H., Kosugi, T., Shiomi, Y., Sawa, M., Kai, K.: 1994, In: Enome, S., Hirayama, T. (eds.) *Proc. Kofu Symposium*, Kofu, Japan, 35.
- Inglis, A.R., Gilbert, H.R.: 2013, *Astrophys. J.* **777**, 30. [ADS](#). [DOI](#).
- Ji, H., Huang, G., Wang, H.: 2007, *Astrophys. J.* **660**, 893. [ADS](#). [DOI](#).
- Ji, H., Huang, G., Wang, H., Zhou, T., Li, Y., Zhang, Y., Song, M.: 2006, *Astrophys. J. Lett.* **636**, L173. [ADS](#). [DOI](#).
- Kallunki, J., Pohjolainen, S.: 2012, *Solar Phys.* **280**(2), 491. [ADS](#). [DOI](#).
- Kliem, B., Karlický, M., Benz, A.O.: 2000, *Astron. Astrophys.* **360**, 715. [ADS](#).
- Kochanov, A.A., Anfinogentov, S.A., Prosovetsky, D.V.: 2013, *Publ. Astron. Soc. Japan* **65**(SP1), S19. [ADS](#). [DOI](#).
- Kosugi, T., Dennis, B., Kai, K.: 1988, *Astrophys. J.* **324**, 1118. [ADS](#). [DOI](#).
- Kundu, M.R., Grechnev, V.V., White, S.M., Schmahl, E.J., Meshalkina, N.S., Kashapova, L.K.: 2009, *Solar Phys.* **260**(1), 135. [ADS](#). [DOI](#).

- Lee, J.W., Gary, D.E., Zirin, H.: 1994, *Solar Phys.* **152**, 409. [ADS](#). [DOI](#).
- Lemen, J.R., Title, A.M., Akin, D.J., Boerner, P.F., Chou, C., Drake, J.D., et al.: 2012, *Solar Phys.* **275**, 17. [ADS](#). [DOI](#).
- Lesovoi, S.V., Altyntsev, A.T., Ivanov, E.F., Gubin, A.V.: 2012, *Solar Phys.* **280**(2), 651. [ADS](#). [DOI](#).
- Lin, R.P., Dennis, B.R., Hurford, G.J., Smith, D.M., Zehnder, A., Harvey, P.R., et al.: 2002, *Solar Phys.* **210**, 3. [ADS](#). [DOI](#).
- Meshalkina, N.S., Altyntsev, A.T., Sych, R.A., Chernov, G.P., Yan, Y.: 2004, *Solar Phys.* **221**, 85. [ADS](#). [DOI](#).
- Mészárosová, H., Karlický, M., Rybák, J., Fárník, F., Jiříčka, K.: 2006, *Astron. Astrophys.* **460**, 865. [ADS](#). [DOI](#).
- Mossessian, G., Fleishman, G.D.: 2012, *Astrophys. J.* **748**(2), 140. [ADS](#). [DOI](#).
- Nakajima, H., Kosugi, T., Kai, K., Enome, S.: 1983, *Nature* **305**, 292. [ADS](#). [DOI](#).
- Nakajima, H., Sekiguchi, H., Sawa, M., Kai, K., Kawashima, S.: 1985, *Publ. Astron. Soc. Japan* **37**, 163. [ADS](#).
- Nakajima, H., Nishio, M., Enome, S., Shibasaki, K., Takano, T., Hanaoka, Y., Torii, C., Sekiguchi, H., Bushimata, T., Kawashima, S.: 1994, *Proc. IEEE* **82**(5), 705. [ADS](#).
- Nakariakov, V.M., Melnikov, V.F.: 2009, *Space Sci. Rev.* **149**, 119. [ADS](#). [DOI](#).
- Nakariakov, V.M., Zimovets, I.V.: 2011, *Astrophys. J. Lett.* **730**, L27, 4 pp. [ADS](#). [DOI](#).
- Nakariakov, V.M., Foullon, C., Verwichte, E., Young, N.P.: 2006, *Astron. Astrophys.* **452**, 343. [ADS](#). [DOI](#).
- Nishio, M., Yaji, K., Kosugi, T., Nakajima, H., Sakurai, T., et al.: 1997, *Astrophys. J.* **489**, 976. [ADS](#).
- Palshin, V.D., Charikov, Yu.E., Aptekar, R.L., Golenetskii, S.V., Kokomov, A.A., Svinkin, D.S., Sokolova, Z.Ya., Ulanov, M.V., Frederiks, D.D., Tsvetkova, A.E.: 2014, *Geomagn. Aeron.* **54**, 943. [ADS](#). [DOI](#).
- Roberts, B., Edwin, P.M., Benz, A.O.: 1984, *Astrophys. J.* **279**, 857. [ADS](#). [DOI](#).
- Shibasaki, K., Ishiguro, M., Enome, S.: 1979, *Proc. Res. Inst. Atmos. Nagoya Univ.* **26**, 117. [ADS](#).
- Simoës, P.J.A., Fletcher, L., Hudson, H.S., Russel, A.J.B.: 2013, *Astrophys. J.* **777**, 152. [ADS](#). [DOI](#).
- Tajima, T., Brunel, F., Sakai, J.: 1982, *Astrophys. J. Lett.* **258**, L45. [ADS](#). [DOI](#).
- Tajima, T., Sakai, J., Nakajima, H., Kosugi, T., Brunel, F., Kundu, M.R.: 1987, *Astrophys. J.* **321**, 1031. [ADS](#). [DOI](#).
- Uralov, A.M., Lesovoi, S.V., Zandanov, V.G., Grechnev, V.V.: 2002, *Solar Phys.* **208**, 69. [ADS](#). [DOI](#).
- Wang, H., Gary, D.E., Zirin, H., Schwartz, R.A., Sakao, T., Kosugi, T., Shibata, K.: 1995, *Astrophys. J.* **453**, 505. [ADS](#). [DOI](#).
- White, S.M., Benz, A.O., Christe, S.: 2011, *Space Sci. Rev.* **159**, 225. [ADS](#). [DOI](#).
- Yang, Y.-H., Cheng, C.Z., Krucker, S., Lin, R.P., Ip, W.H.: 2009, *Astrophys. J.* **693**, 132. [ADS](#). [DOI](#).
- Zhdanov, D.A., Zandanov, V.G.: 2011, *Cent. Eur. Astrophys. Bull.* **35**, 223. [ADS](#).